Catalytic CO 2 Reduction with Heptacoordinated Polypyridine Complexes: Switching the Selectivity via Metal Replacement

Federico Droghetti, Agnese Amati, Fabien Pascale, Aurélien Crochet, Mariachiara Pastore, Albert Ruggi, Mirco Natali

Catalytic CO_2 Reduction with Heptacoordinated Polypyridine Complexes: Switching the Selectivity via Metal Replacement

Federico Droghetti,[a] Agnese Amati,[a] Fabien Pascale,[b] Aurélien Crochet,[c] Mariachiara Pastore,*[b] Albert Ruggi,*[c] Mirco Natali *[a]

[a] F. Droghetti, A. Amati, M. Natali
Department of Chemical, Pharmaceutical and Agricultural Sciences
University of Ferrara
Via L. Borsari 46, 44121, Ferrara, Italy.
E-mail: mirco.natali@unife.it

[b] F. Pascale, M. Pastore
Laboratoire de Physique et Chimie Théoretiques
University of Lorraine & CNRS
54000 Nancy, France.
E-mail: mariachiara.pastore@univ-lorraine.fr

[c] A. Crochet, A. Ruggi
Department of Chemistry
University of Fribourg
Chemin du Musée 9, 1700 Fribourg, Switzerland.
E-mail: albert.ruggi@unifr.ch

Supporting information for this article is given via a link at the end of the document.

Abstract: The discovery of molecular catalysts for the CO_2 reduction reaction (CO_2RR) in the presence of water, which are both effective and selective towards the generation of carbon-based products, is a critical task in the realm of Artificial Photosynthesis. Herein we report the catalytic activity towards the CO_2RR by a cobalt complex (**1**) and its iron analog (**2**) both featuring the same redox-active ligand and an unusual seven-coordination environment. Electrochemical experiments in CO_2-saturated acetonitrile/water mixtures show that the cobalt complex mainly yields formate (applied potential of −2.0 V vs Fc^+/Fc and 1% H_2O) or H_2 (at higher applied bias or water content), while the iron complex always delivers CO as the major product. The different catalytic activity is further confirmed under photochemical conditions using $[Ru(bpy)_3]^{2+}$ as the sensitizer and DIPEA as the electron donor, where **1** behaves as a selective catalyst towards H_2 formation, while **2** quantitatively generates CO. This is ascribed to a preference towards a metal-hydride pathway for the cobalt complex vs. a metal-carboxyl pathway for the iron analog. These results highlight how a simple metal replacement may have a profound impact on the reactivity of transition metal complexes towards solar fuel formation.

Introduction

The continuous emission of greenhouse gases by human activities is currently causing severe environmental issues. In this regard, the transformation of CO_2 into reduced carbon forms, such as fuels or industrially relevant intermediates, represents a great challenge.[1-4] CO_2 reduction is, however, a complex reaction. A large energy requirement is indeed associated with the formation of the $CO_2^{\bullet-}$ radical anion via a one-electron transfer process (eq. 1, E = −2.21 V vs. SCE in DMF).[5] This energy penalty can be decreased substantially in the presence of a proton donor (eqs. 2-6),[6] but at the expense of large kinetic barriers associated with the multiple exchanges of electrons and protons. Besides, the introduction of protons in the reaction media may trigger the parallel hydrogen evolving reaction (HER, eq. 7) which may compete with the targeted CO_2 reduction reaction (CO_2RR).

$$CO_2 + e^- \rightarrow CO_2^{\bullet-} \quad (1)$$
$$CO_2 + 2\,H^+ + 2\,e^- \rightarrow CO + H_2O \quad (2)$$
$$CO_2 + 2\,H^+ + 2\,e^- \rightarrow HCO_2H \quad (3)$$
$$CO_2 + 4\,H^+ + 4\,e^- \rightarrow H_2CO + H_2O \quad (4)$$
$$CO_2 + 6\,H^+ + 6\,e^- \rightarrow CH_3OH + H_2O \quad (5)$$
$$CO_2 + 8\,H^+ + 8\,e^- \rightarrow CH_4 + 2\,H_2O \quad (6)$$
$$2\,H^+ + 2\,e^- \rightarrow H_2 \quad (7)$$

According to these considerations, the identification of active and selective catalysts for the CO_2RR currently represents a critical task. In this regard, molecular catalysts based on transition metal complexes have received considerable interest due to their great versatility and tunability over heterogeneous materials. Examples of this kind include rhenium and ruthenium complexes[7-16] as well as complexes of Earth-abundant metals,[17-44] whose activity mainly results in the generation of CO or formate (eqs. 2,3).
The ability of first-row transition-metal polypyridine complexes to catalyze the CO_2RR has been long studied during the last decade starting from seminal works by Fontecave and co-workers on terpyridine complexes[45,46] as well as by Deronzier and coworkers

on Mn(I) R-bpy-carbonyl complexes (where R-bpy = substituted 2,2'-bipyridine).[47,48] In the following studies, ligand design has represented the major target, aiming to lower the overpotential and improve both catalytic rates and selectivity towards carbon-based products. In this respect, redox non-innocent ligands have been frequently employed, due to the general idea that decreasing the electronic density on the metal center would lower the thermodynamic potential for the catalyst reduction, thus decreasing the overpotential required for catalysis, and hamper the formation of metal-hydride species, thus leading to selective CO_2RR over the competitive HER.[49,50] However, the benefit of this approach was not as general as expected.[51] The use of redox-active ligands was indeed observed in some cases to either open to undesired reactivity and loss of activity[52-54] or to be characteristic of specific transition metals.[50]

During the last years, we have been interested in the design and application of cobalt complexes as catalysts for the HER.[55-62] In particular, we have reported on the hydrogen evolution activity by cobalt polypyridine complexes featuring the redox-active, hexadentate DBPy-PyA ligand, where DBPy-PyA = (1-([2,2'-bipyridin]-6-yl)-N-([2,2'-bipyridin]-6-ylmethyl)-N-(pyridin-2-ylmethyl)methanamine, and synthetic variations thereof.[63-67]

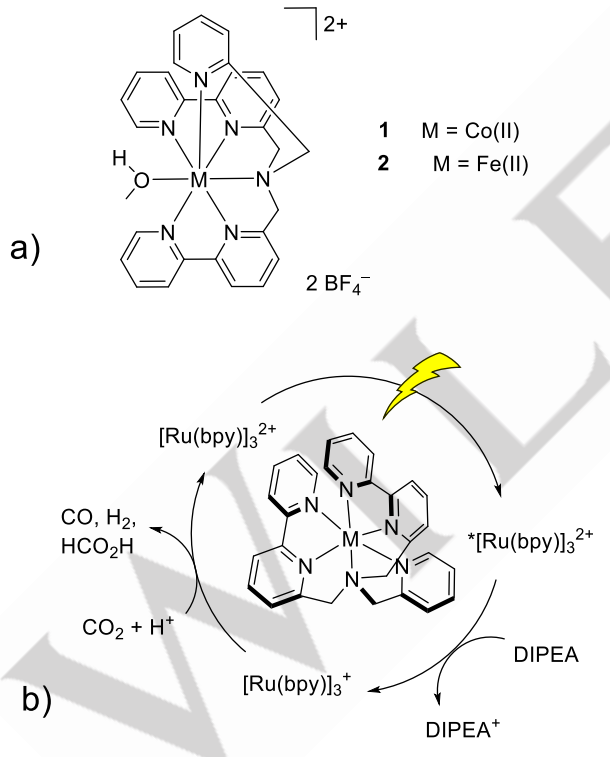

Scheme 1. a) Molecular structure of complexes **1** and **2** used as catalysts and b) schematic representation of the photochemical system employed in this work (where DIPEA = N,N-diisopropylethylamine).

These complexes display a peculiar heptacoordinated structure in the solid state which is rather uncommon for first-row transition metal complexes. Despite the absence of a free coordination site, the complexes showed high activity towards the HER, particularly when catalysis was driven by photochemical means in acidic aqueous solutions in the presence of $[Ru(bpy)_3]^{2+}$ (where bpy = 2,2'-bipyridine) as the sensitizer and ascorbate as the sacrificial electron donor.[63,65,67] As a matter of fact, the ligand is substantially flexible to suitably accommodate the different oxidation states of the cobalt during the HER catalysis and the external pyridine ligand(s) can detach from the metal center under turnover conditions to provide internal proton relays enabling proton transfer steps via intramolecular routes.[64] The presence of biomimetic acid-base functionalities in the catalyst platform has been indeed demonstrated to be a fundamental prerequisite to promote fast and efficient catalysis for both proton and CO_2 reduction.[68,69]

Starting from these premises we have decided to extend the scope of our investigation toward the CO_2RR. We report herein the comparison of the catalytic activity by the prototype cobalt complex (**1**) and the novel iron analog (**2**) in acetonitrile/water mixtures under both electrochemical and light-driven conditions using a standard photochemical system (Scheme 1). Interestingly, while the investigation of the cobalt complex under the experimental conditions relevant to the CO_2RR still confirms its preference towards a hydride pathway leading to the generation of formate and/or H_2, a simple replacement of the cobalt center with iron allows the achievement of high selectivity towards the formation of CO.

Results and Discussion

Synthesis and Characterization

The cobalt complex **1**, available from previous studies,[63-67] was prepared by treatment of the hexadentate DBPy-PyA ligand with $Co(BF_4)_2{\cdot}6H_2O$ in a methanol solution and subsequent precipitation with diethyl ether. The absorption spectrum in acetonitrile solution (Figure S1) shows two bands in the visible region (attenuation coefficients of $\varepsilon \sim 40\ M^{-1}cm^{-1}$) with maxima at 450 and 505 nm and a shoulder at longer wavelengths, assigned to d-d transitions involving the cobalt(II) center. Upon addition of water, only minimal spectral changes can be observed (Figure S1). As previously pointed out,[65] this observation can be taken as an indication that in solution the seventh, weakly bound methanol ligand is displaced, leading to a six-coordinated cobalt(II) complex in a distorted octahedral geometry.

The iron complex **2** was obtained similarly by reaction of the DBPy-PyA ligand with $Fe(BF_4)_2{\cdot}6H_2O$ and characterized using complementary techniques. Single crystals of complex **2**, suitable for X-ray diffraction, were obtained by slow diffusion of diethyl ether in a methanol solution of **2**. The solid-state structure is shown in Figure 1, together with the coordination polyhedron, while the crystallographic parameters are collected in the SI (see Section S2). The complex displays a heptacoordinated geometry which can be described as a faced capped octahedron. Six coordination positions are occupied by the hexadentate DBPy-PyA ligand and the seventh position is occupied by a molecule of methanol. The closest to linear angles are N6-Fe-N1 and O1-Fe-N4, with bond angles of 161.05(19)° and 160.68(19)°, respectively. Fe-N bond lengths are in the range of 2.14-2.35 Å, the longest bond being the one between Fe and the tertiary amine

(Fe-N3, 2.35 Å). These bond distances are in line with the average Fe-N bond distance typically observed in Fe(II) complexes (2.08 ± 0.055 Å, see Figure S4 in the SI). It is worth mentioning that heptacoordinated Fe(II) complexes including six N-containing heteroaromatic ligands are extremely rare: only 57 examples are known, of which only 8 present an oxygen atom as the seventh donating ligand.[70] The Bond Valence Sum (BVS) method gave a value of 1.914, in agreement with the valence of Fe(II).[71,72]

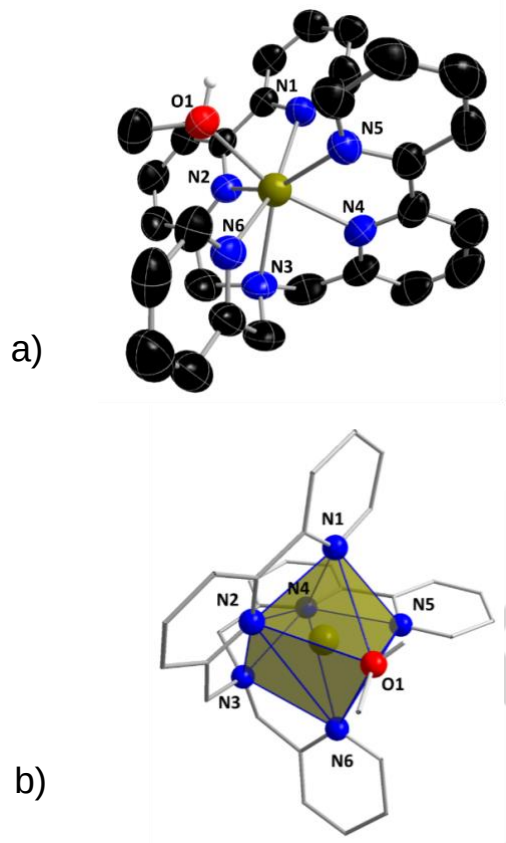

Figure 1. a) ORTEP drawing and b) coordination polyhedron of complex **2** obtained from single-crystal X-ray diffraction analysis.

The absorption spectrum of complex **2** in acetonitrile (Figure S2) displays an intense band in the visible ($\varepsilon \sim 800\ M^{-1}cm^{-1}$) with a maximum at 476 nm, which can be attributed to a metal-to-ligand charge-transfer (MLCT) transition. Upon addition of water, a red shift can be observed, accompanied by two isosbestic points at 415 and 505 nm, with the new band featuring a maximum at 494 nm (Figure S2). These spectral changes can be explained by considering the replacement of the apical methanol ligand with acetonitrile after dissolution in the aqueous-free solvent and substitution of the acetonitrile ligand with H_2O upon increasing the water content. The spectral red-shift of the MLCT band is indeed consistent with the higher electron-donating character of water than acetonitrile. The magnetic properties of complex **2** in solution were studied by the Evans method in an acetonitrile-d_3 solution containing 1% tetramethylsilane (TMS) (Figure S3).[73] A magnetic moment μ_{calc} = 4.95 BM was obtained, indicating a high-spin complex with four unpaired electrons in the ground state.

As evident from the comparison of the structural properties (Section S2 of the SI, Tables S1-S3), complexes **1** and **2** show several remarkable affinities: i) they have indeed a heptacoordinated geometry with very similar bond distances and angles, ii) they show a BVS < 2, suggesting an insufficient coordination of the metal center to the ligand sphere, and iii) they show a high spin configuration of their ground state in solution.

Consistent with the experimental evidence of a high-spin ground state in complex **2**, DFT calculations at the B3LYP/6-311G* level in acetonitrile converge to a quintet ground state (S = 2, spin density of 3.79 and a Mulliken charge of 1.52 on the iron) characterized by a seven coordination environment around the iron(II) center in a capped octahedral geometry involving the DBPy-PyA chelate with an elongated Fe-N(amine) bond and an acetonitrile molecule (see Section S3 of the SI for further details). As depicted in Figure S7, the TD-DFT absorption spectrum (see listed transitions in Table S5) well reproduces the appearance of two bands, as experimentally observed (Figure S2). The lowest energy absorption predicted is characterized by MLCT transitions and is slightly red-shifted with respect to the experimental one. The underestimation of the excitation energy of charge transfer states is not surprising for the B3LYP method,[74] which, however, allows an overall balanced description of the considered system (viz. structures, electronic structure, optical properties).[75,76] Interestingly, a bathochromic shift is also predicted by TD-DFT calculations for the analog complex **2** with a water molecule as the monodentate ligand (Figure S7), thereby corroborating the presumed ligand exchange at higher H_2O content.

The electrochemical properties of both compounds **1** and **2** were then examined by cyclic voltammetry (CV) under N_2. Complex **1** in acetonitrile shows two reduction waves of reversible nature upon cathodic scan, featuring half-wave potentials of −1.50 and −2.06 V vs. Fc^+/Fc (Figure 2a). As previously reported,[64] spin density and Mulliken charge analyses of the one- and two-electron reduced species highlight that the first reduction process, associated with a formal Co(II)/Co(I) reduction hereafter, involves the cobalt center and one bipyridine ligand, while the second reduction step at more negative potentials, associated with a formal Co(I)/Co(0) reduction hereafter, occurs mainly on the ligand. No relevant oxidation processes were observed upon anodic scan.[63]

Upon cathodic scan, the CV of the iron(II) complex **2** in acetonitrile exhibits two reduction features of reversible character occurring at half-wave potentials of −1.65 and −1.85 V vs. Fc^+/Fc (Figure 2), associated with formal Fe(II)/Fe(I) and Fe(I)/Fe(0) processes hereafter, respectively. For both redox waves the current varies linearly with the square root of the scan rate (Figure S10), as expected for diffusion-controlled processes.

Spectroelectrochemical experiments in N_2-purged acetonitrile were then performed to characterize the one- and two-electron reduced species of complex **2**. The differential absorption spectra are reported in Figure 2b. The electrogeneration of the Fe(I) species is accompanied by depletion of the MLCT absorption characteristic of the pristine complex and the concurrent formation of two main absorption bands with maxima at 385 and 575 nm. The formation of the Fe(0) species, on the other hand, is associated with an enhancement of both absorption patterns, a

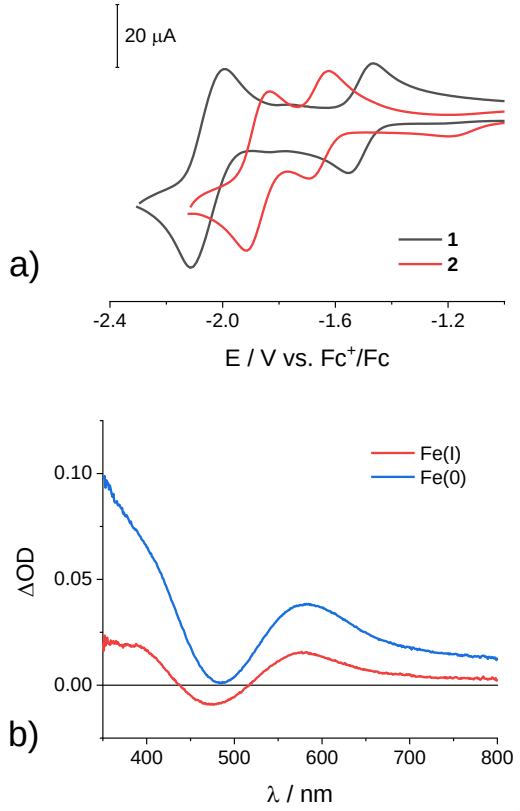

Figure 2. a) CV of complexes **1** and **2** recorded at room temperature in N_2-purged acetonitrile with 0.1 M $TBAPF_6$ as the supporting electrolyte at a scan rate of 0.1 V/s with a glassy carbon as the working electrode; b) differential absorption spectra of the electrogenerated Fe(I) and Fe(0) species obtained by spectroelectrochemistry of **2** (applied potential of −1.7 and −2.0 V vs Fc^+/Fc, respectively) in N_2-purged acetonitrile with 0.1 M $TBAPF_6$ as the supporting electrolyte.

decrease of the MLCT bleach, and a slight red-shift of the low-energy transition (maximum at 584 nm). Interestingly, similar spectral changes were observed for the one-electron reduced species of a related iron complex and assigned to localization of the reduction equivalent onto the polypyridine ligand.[77] This evidence therefore supports a relevant ligand-based nature of both the one-and two-electron reduced species in complex **2**.

Consistent with these experimental findings, DFT calculations indicate that both reductions are mostly localized on the DBPy-PyA ligand. For the first reduction, a potential of −1.49 V vs. Fc^+/Fc is predicted, which is appreciably close to the value experimentally determined. Analysis of the redox-active orbitals demonstrates only a partial involvement of the iron center (11%) and a major contribution of one bipyridine (Figure 3a-c). The resulting Fe(I) species is predicted as an antiferromagnetic quartet ground state (S = 3/2) with a spin density of 3.71 and a Mulliken charge of 1.48 on the metal center. The calculated exchange coupling constant between the antiferromagnetic and ferromagnetic (S = 5/2) states is 283 cm^{-1}, corresponding to a gap of 1180 cm^{-1} between the high and low spin states. Structural optimization shows that the Fe(I) species still retains the heptacoordination around the iron with a bound acetonitrile ligand. As for the second reduction, DFT calculations predict a potential of −1.94 V vs. Fc^+/Fc, in close agreement with the experimental value. The analysis of the redox-active orbitals suggests that the second electron is almost completely delocalized onto the hexadentate DBPy-PyA ligand. The resulting Fe(0) species is predicted as an antiferromagnetic triplet ground state (S = 1) with a spin density of 3.68 and a Mulliken charge of 1.44 on the metal center (Figure 3d-f). The ferromagnetic-antiferromagnetic gap was calculated as 1179 cm^{-1} with an exchange coupling constant of 217 cm^{-1}. Structural optimization indicates the removal of the apical acetonitrile ligand and a six-coordination environment around the iron in a distorted trigonal prismatic geometry.

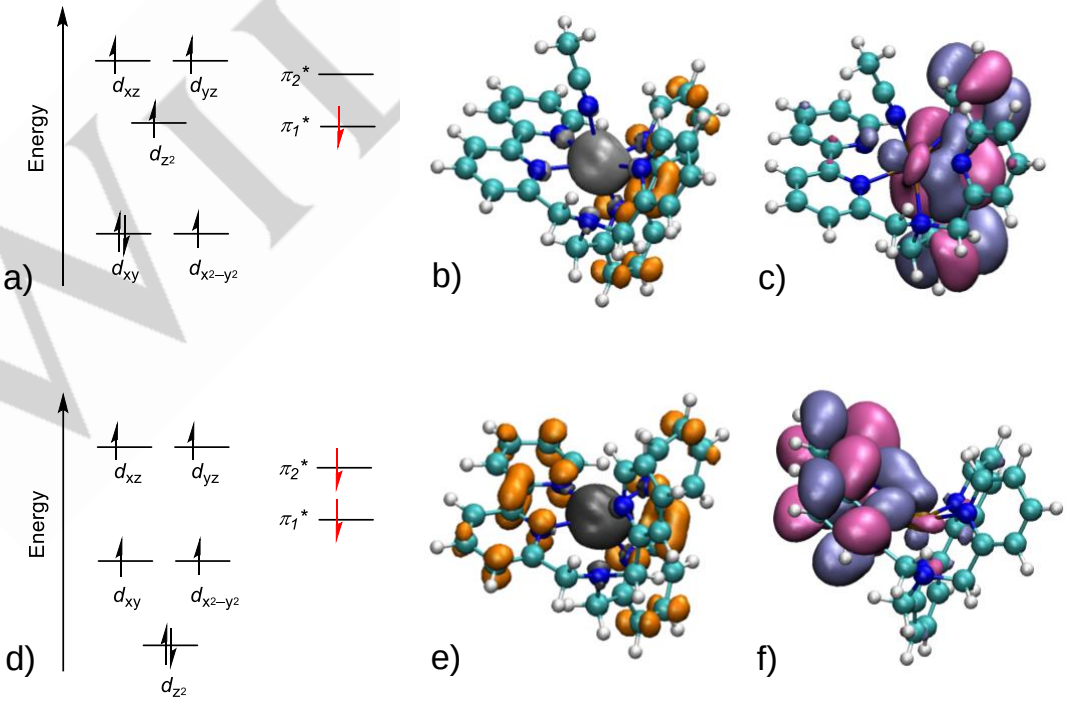

Figure 3. Simplified MO diagram, spin density plot and redox active orbitals calculated by DFT on the one-electron reduced Fe(I) species (a,b,c) and two-electron reduced Fe(0) species (d,e,f).

Notably, the absorption spectra of both the Fe(I) and Fe(0) species calculated by TD-DFT (Figure S9) well match the spectral variations obtained by spectroelectrochemical analysis (Figure 2b), thus validating the theoretical protocol and the electronic structures of the reduced species. As depicted in Figure S9, indeed, the appearance of intense absorptions around 600 and 380 nm is predicted for both Fe(I) and Fe(0), with the lowest-energy one slightly red-shifted in the case of Fe(0), which also shows a small absorption feature at ca 510 nm.

Under anodic scan the iron complex **2** in pure acetonitrile undergoes oxidation at a potential of +0.42 V vs. Fc^+/Fc (Figure S11), associated with a metal-centered Fe(II)/Fe(III) one-electron process. Interestingly, this oxidation experiences a cathodic shift by ca 0.15 V upon increasing the water content up to 10% (Figure S12), consistent with the spectral variations previously discussed (Figure S2). On the other hand, all the reduction features are apparently insensitive to the presence of water, suggesting negligible reactivity of the electrogenerated Fe(I) and Fe(0) species with the latter proton donor.

Electrocatalytic CO_2 Reduction

The electrochemical response of both complexes **1** and **2** in acetonitrile undergoes peculiar changes when the solution is saturated with CO_2 (0.28 M in acetonitrile).[78] In the case of complex **1** (Figure 4a), the Co(II)/Co(I) reduction wave increases only slightly in current (i_{cat}/i_p = 1.2) suggesting weak reactivity of the electrogenerated Co(I) species, as confirmed by the appreciable reversibility of the redox wave upon scan reversal at −1.65 V vs Fc^+/Fc. On the other hand, two new redox features, absent in N_2, can be observed upon further cathodic scan. A first reduction wave starts at more positive potentials than the Co(I)/Co(0) reduction (half-wave potential of $E_{cat,1}$ = −1.93 V vs Fc^+/Fc, estimated at the inflection point of the wave)[79] and exhibits a substantial current enhancement when compared to the redox process in the absence of the CO_2 substrate (i_{cat}/i_p = 4.9), consistent with a catalytic process. The anodic shift suggests the occurrence of a fast chemical reaction involving the electrogenerated Co(0) species and the CO_2 molecule,[80] according to an EC mechanism (where E and C are an electron transfer and a chemical step, respectively), while the current increase is assigned to catalytic CO_2 reduction. This very likely occurs through an EECC mechanism,[81] in which the CO_2 molecule works as both the substrate and the oxide acceptor.[82]

A second reduction wave is then observed at more negative potentials (half-wave potential of $E_{cat,2}$ = −2.19 V vs Fc^+/Fc, current enhancement i_{cat}/i_p = 8.9), still assignable to catalytic CO_2 reduction. For this latter, an alternative mechanism can be envisioned, likely involving coordination of the CO_2 substrate to a cobalt-carbonyl intermediate which has not turned over during the first catalytic event.[82] Consistent with this hypothesis, two anodic processes can be distinguished at ca −1.5 and −0.9 V vs Fc^+/Fc during the return scan (see inset in Figure 4a), assignable to oxidation of cobalt-carbonyl species.[82] Interestingly, the measured currents for each oxidation process are strongly dependent on the potential at which the scan is reversed, thus suggesting that different carbonyl intermediates can be attained depending on whether the cathodic scan is directed only to the first catalytic wave or proceeds down to the second catalytic event. Addition of increasing amounts of water in the presence of CO_2 (Figure 4b) triggers a substantial enhancement of the catalytic currents at potentials below −1.7 V vs Fc^+/Fc, with the two catalytic events observed in anhydrous conditions almost collapsing into a single one at high water content. These observations suggest that water can accelerate catalytic CO_2 reduction mediated by the cobalt complex. However, it should be noticed that the half-wave potentials $E_{cat,1}$ and $E_{cat,2}$ change as a function of both the water concentration and scan rate (Figures S13-S19), indicating an odd catalytic behavior of complex **1** with respect to the CO_2RR with water as the proton donor, likely involving a competition among different reduction processes. Consistently, a proportional current enhancement upon addition of water is detected even in the absence of CO_2 (Figure S20), confirming the potential reactivity of the electrogenerated Co(0) species with weak acids.[64]

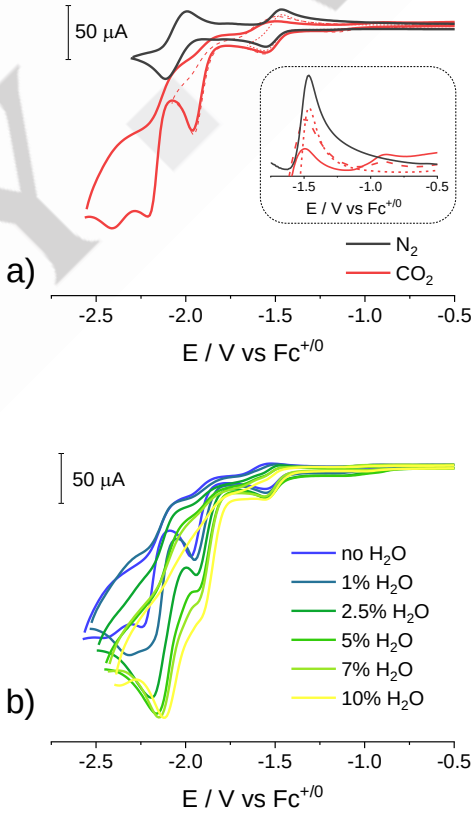

Figure 4. CV of 1 mM complex **1** in acetonitrile a) under N_2 or CO_2 (inset: zoom of the anodic scan) and b) under CO_2 at different water content; CVs were recorded at 0.1 V/s with a glassy carbon as the working electrode with 0.1 M $TBAPF_6$ as the supporting electrolyte.

Addition of CO_2 to an acetonitrile solution containing complex **2** (Figure 5a) triggers a current enhancement at both the Fe(II)/Fe(I) and Fe(I)/Fe(0) reduction waves (i_{cat}/i_p = 1.4 and 3.0, respectively), consistent with the ability of both electrogenerated Fe(I) and Fe(0) to activate CO_2. More importantly, addition of H_2O enables a current increase at both waves (Figure 5b), associated with

favorable CO_2 activation and concurrent catalysis in the presence of a proton donor. The scan rate dependence of the electrocatalytic response of **2** was then examined (Figures S21-S26). Interestingly, the catalytic wave at less negative potentials becomes reversible upon increasing the scan rate, indicating a sluggish electrocatalytic reaction associated with the Fe(I) species. More importantly, for both catalytic processes, the potentials of the catalytic waves ($E_{cat,1}$ and $E_{cat,2}$, respectively, calculated at the inflection point)[79] are constant with increasing concentration of H_2O and scan rate, and identical to the half-wave potentials of the Fe(II)/Fe(I) and Fe(I)/Fe(0) reductions, respectively, in the absence of the CO_2 substrate (Figure S27). These experimental evidences, combined with the negligible reactivity of the electrogenerated Fe(I) and Fe(0) species with water, as detected by CV analysis (Figure S12), strongly suggest a preferential reactivity of catalyst **2** towards the CO_2RR to CO.

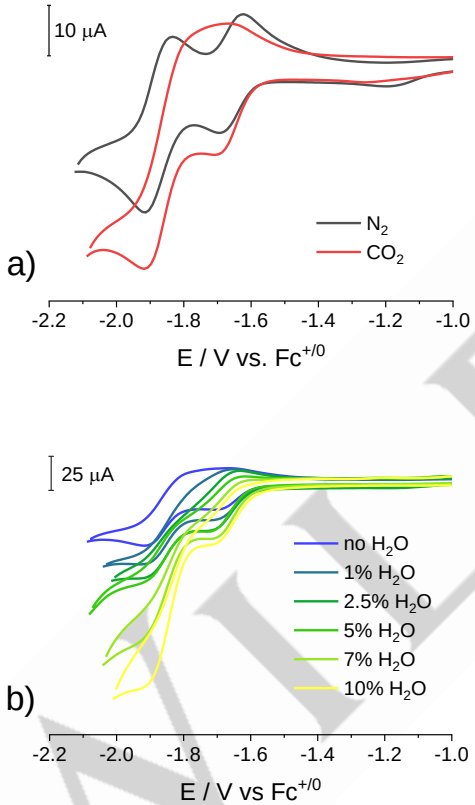

Figure 5. CV of 1 mM complex **2** in acetonitrile a) under N_2 or CO_2 and b) under CO_2 at different water content; CVs were recorded at 0.1 V/s with a glassy carbon as the working electrode with 0.1 M $TBAPF_6$ as the supporting electrolyte.

Bulk electrolysis experiments were then performed to establish and quantify the products of catalysis by both complexes **1** and **2** in CO_2-saturated acetonitrile solutions at two different water contents, namely 1% and 10%. Figure 6 collects the Faradaic efficiencies (FEs) for the formation of CO, formate, and H_2 after 2 h electrolysis attained at two different potentials corresponding to the main catalytic events in either cases (see Table 1 for the numerical data). Inspection of the data shows that, upon application of −2.0 V vs Fc^+/Fc, complex **1** is rather selective towards the reduction of CO_2 only in the presence of 1% H_2O, leading to an overall 84% of carbon-based products (formate + CO) with a major content in formate (52%). However, upon increasing the concentration of water up to 10%, hydrogen is attained as the major product with a selectivity of 55%. On the other hand, electrolysis at −2.3 V vs Fc^+/Fc with complex **1** yields hydrogen as the main reduction product regardless of the water content present (selectivity of 63% and 86% at 1% and 10% H_2O, respectively).

Complex **2** is instead extremely active towards the generation of carbon-based products (formate + CO) at all applied potentials, with selectivity values of >99% and >94% in the presence of 1% and 10% H_2O, respectively. In particular, the iron catalyst **2** is highly selective towards the generation of CO with values of >78% and >74% at 1% and 10% H_2O, respectively. These results highlight how effective is the simple metal replacement in switching the catalytic activity.

For both complexes **1** and **2**, the "unpolished electrode" test performed after 2 h bulk electrolysis confirms that the observed catalysis is not due to heterogeneous species formed at the electrode surface.[26] Negligible currents, associated with only trace amounts of H_2, were indeed measured upon electrolysis of a catalyst-free solution using a GC electrode previously employed for electrolysis tests with either **1** or **2**.

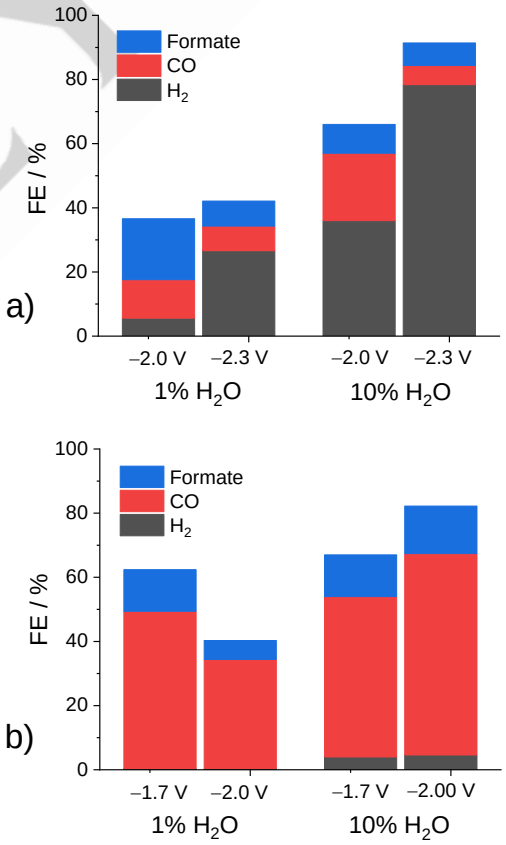

Figure 6. Faradaic efficiencies for formate, CO, and H_2 obtained after 2 h electrolysis of CO_2-saturated acetonitrile solutions (0.1 M $TBAPF_6$ as the supporting electrolyte) containing a) 1 mM **1** and b) 1 mM **2** with different concentrations of water (1-10%) and at different applied potentials.

Table 1. Summary of bulk electrolysis data in acetonitrile.[a]

		Faradaic Efficiency / %			Selectivity [e] / %		
Cat	H_2O / %	H_2	CO	Formate	H_2	CO	Formate
1[b]	1	6	12	19	16	32	52
1[c]	1	27	8	8	63	18.5	18.5
1[b]	10	36	21	9	55	32	13
1[c]	10	78	6	7	86	6.5	7.5
2[d]	1	0.4	49	13	0.6	78.6	20.8
2[b]	1	0.3	34	6	0.7	84.3	15
2[d]	10	4	50	13	6	74.6	19.4
2[b]	10	4.5	63	15	5.5	76.5	18

[a] estimated after 2 h, 1 mM catalyst concentration, CO_2-saturated solution, 0.1 M $TBAPF_6$, GC as working electrode, Pt as the counter electrode, SCE as the reference, potentials converted vs Fc^+/Fc by subtracting 0.4 V; [b] applied potential −2.0 V vs Fc^+/Fc; [c] applied potential −2.3 V vs Fc^+/Fc; [d] applied potential −1.7 V vs Fc^+/Fc; [e] estimated as the ratio between the amount of each product and the total amount of products.

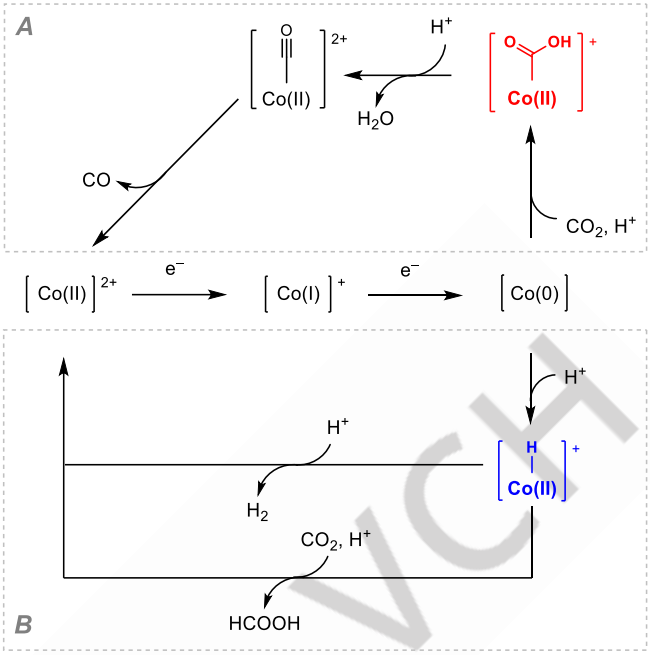

Scheme 2. Proposed catalytic mechanisms for CO_2 and proton reduction in acetonitrile/water solution by complex **1**: A) carboxyl and B) hydride pathways.

A critical inspection of the CV and bulk electrolysis data was then made in order to discuss the different reactivity of complexes **1** and **2** towards CO_2RR in acetonitrile/water mixtures. For complex **1**, CV analysis clearly shows the requirement of two electron-transfer processes, with the generation of the reduced Co(0) species, before the occurrence of any relevant chemical steps. For electrocatalysis promoted at the lowest applied potentials (i.e., −2.0 V vs Fc^+/Fc), the positive shift of the catalytic wave supports rapid CO_2 binding at the Co(0) species, leading to the formation of a carboxyl intermediate (Scheme 1, pathway A). Subsequent protonation and release of a water molecule result in the generation of a cobalt(II) carbonyl. CO elimination finally restores the initial Co(II) species, ready to enter a new catalytic cycle.[46] In the presence of water and/or carbonic acid (resulting from CO_2 bubbling in water),[83] however, the observed current enhancement (Figure S20) suggests that Co(0) can also undergo protonation, leading to the formation of a cobalt(II) hydride species (Scheme 1, pathway B). This represents the starting point to achieve either formate, by hydride transfer to the CO_2 molecule, or hydrogen, by proton-aided heterolytic cleavage of the cobalt-hydride bond. The observation in the bulk electrolysis experiments at −2.0 V vs Fc^+/Fc of larger yields in formate (at 1% water) or hydrogen (at 10% water) than CO demonstrates that pathway B is strongly preferred over pathway A using water as the proton donor. The change in the major reaction product upon increase of the water content can be ascribed to the different mutual concentrations of the hydride-accepting species (i.e., CO_2 or H^+) in the two conditions. On the other hand, the high yields in hydrogen achieved with **1** at more negative potentials (−2.3 V vs Fc^+/Fc) can be related to a parallel catalytic mechanism, likely implying an additional reduction of the metal complex. This would potentially lead to an even more electron-rich cobalt center, thus possibly enhancing the reactivity towards protons.

The bulk electrolysis experiments with **2** show that the iron complex turns out to be a highly selective catalyst towards CO_2 reduction to CO. CV analysis shows current enhancement at both the Fe(II)/Fe(I) and Fe(I)/Fe(0) reductions, highlighting two operative mechanisms for CO formation, as depicted in Scheme 3 (pathway A). The catalytic wave at less negative potentials grows up at the Fe(II)/Fe(I) process, suggesting that CO_2 addition can occur at the electrogenerated Fe(I) species, with catalysis thus proceeding via an ECEC mechanism involving the generation of a formal Fe(III)-carboxyl intermediate (Scheme 3, pathway A, dashed lines). Subsequent reduction produces a formal Fe(II)-carboxyl moiety from which protonation and water removal eventually bring to the iron(II) carbonyl intermediate. Due to the relatively high stability of these carbonyl compounds, a further reduction is expected to take place before CO elimination.[85] For this ECEC process, the nice match between the potential of the catalytic wave ($E_{cat,1}$) and the half-wave potential of the Fe(II)/Fe(I) reduction in the absence of the CO_2 substrate (Figure S27) suggests that the first chemical step (viz., coordination of CO_2 to the Fe(I) species) is rate-limiting.[84] For this ECEC mechanism, an overpotential of η = 0.31 V can be estimated, considering the $E_{cat,1}$ value and the thermodynamic potential of CO_2RR to CO in aqueous acetonitrile (–1.34 V).[83] Using the electrolysis data attained in CO_2-saturated acetonitrile at 10% H_2O at −1.7 V vs Fc^+/Fc, a TOF = 0.3 s^{-1} can also be extracted (see SI).[80] This modest value can account for the gain in reversibility of the first catalytic wave of **2** observed in the CV experiments upon increasing the scan rate (Figure S21-S26). The catalytic wave at more negative potentials, on the other hand, starts at the Fe(I)/Fe(0) process, suggesting addition of CO_2 to the electrogenerated Fe(0) species and an overall EECC mechanism, involving similar catalytic intermediates (Scheme 3, pathway A, solid lines). Even in this case the value measured for the half-

wave catalytic potential ($E_{cat,2}$) matches the redox potential of the Fe(I)/Fe(0) couple in the absence of CO_2, indicating that the first chemical process (viz., coordination of the CO_2 substrate to the Fe(0) species) represents the rate-determining step.[84] For this EECC mechanism, an overpotential of η = 0.51 V can be estimated[83] and a TOF = 2.2 s^{-1} is extracted from bulk electrolysis data at 10% H_2O at an applied potential of −2.0 V vs Fc^+/Fc (see SI).[80] In a parallel scenario (Scheme 3, pathway B), the Fe(0) might also bind a proton yielding an iron(II)-hydride species.[85] The reaction of this latter with either a proton or a CO_2 molecule eventually leads to hydrogen or formate, respectively. Differently from the cobalt case, the high selectivity towards CO formation recorded employing **2** as the catalyst and the observed negligible reactivity of the Fe(0) species with water (Figure S12) definitely point towards a net preference for pathway A over pathway B.

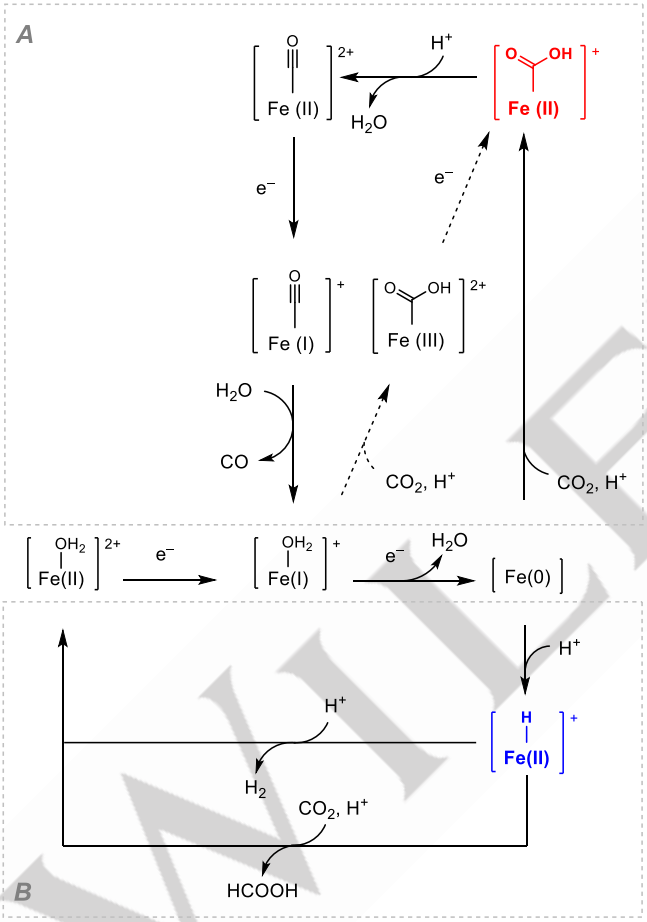

Scheme 3. Proposed catalytic mechanisms for CO_2 and proton reduction in acetonitrile/water solution by complex **2**: A) carboxyl and B) hydride pathways.

In order to shine light on the different catalytic behavior of **1** and **2**, we employed DFT calculations to compute the structures of the relevant catalytic intermediates formed upon reaction of the Co(0) and Fe(0) with either CO_2 or H^+, namely Co(II)-COOH and Co(II)-H (Scheme 2) and Fe(II)-COOH and Fe(II)-H (Scheme 3). The relevant structural parameters as well as the optimized molecular structures are reported in the SI (Section S3). From these data, we were able to extract the driving forces of the formation of both the carboxyl and hydride intermediates for both the cobalt and iron complexes (see Experimental Section). Interestingly, for complex **1**, ΔG values of −18.5 and −17.5 kcal/mol can be estimated for CO_2 binding and protonation, respectively, suggesting a high reactivity of the Co(0) species with both substrates. These data well correlate with the poor selectivity registered for the CO_2RR catalysis in acetonitrile/water mixtures by the cobalt complex **1.** For this latter, however, the greater preference towards the hydride pathway can be ascribed to its ability to mediate proton transfer events via intramolecular routes by taking advantage of the weak bonds between the cobalt centers and the terminal pyridines following reduction of the metal complex.[64] This was indeed recognized as the key figure-of-merit of **1** and related derivatives to account for the high catalytic activity towards photochemical HER in aqueous solutions.[62-67]

On the other hand, a more pronounced reactivity towards CO_2 is found for the iron complex **2** (ΔG = −13.2 and −9.0 kcal/mol for the formation of Fe(II)-COOH and Fe(II)-H, respectively). These data corroborate the strong selectivity registered for complex **2** towards CO formation. This may be partly attributed to the enhanced delocalization of the redox equivalents over the aromatic ligands upon one- and two-electron reduction,[49] highlighting the fundamental role of the redox-active DBPy-PyA ligand. This would indeed make the iron center less prone to proton attack and hydride formation (pathway B) thus favoring CO_2 activation and catalysis towards the desired CO product (pathway A).[49,50] It should be, however, noted that these hypotheses are solely based on thermodynamic aspects and the assessment of the kinetic barriers for both CO_2 and proton coordination is required to reach a definite conclusion.

Light-driven CO_2 Reduction

The ability of complexes **1** and **2** to promote CO_2 reduction was further investigated under photochemical conditions in acetonitrile/water mixtures using $[Ru(bpy)_3](PF_6)_2$ as the sensitizer and DIPEA as the sacrificial electron donor. Within this photochemical system activation of the catalyst is expected to occur via reductive quenching of the excited state of the $[Ru(bpy)_3]^{2+}$ sensitizer by DIPEA (eqs. 8,9) followed by electron transfer from the photogenerated chromophore to the metal complex (C) either in its pristine or one-electron reduced form (eq. 10). As a matter of fact, negligible quenching of the $*[Ru(bpy)_3]^{2+}$ emission was observed in the presence of both complexes **1** and **2** at concentrations ≤ 50 μM, whereas DIPEA can quench the luminescence of $*[Ru(bpy)_3]^{2+}$ with a bimolecular rate constant of $6.6 \cdot 10^6$ $M^{-1}s^{-1}$, as determined by Stern-Volmer analysis (Figure S28). We should also consider that in these experiments the oxidation product of DIPEA (eq 9) is expected to undergo deprotonation and formation of a radical species which may also play the role of reducing agent towards the generation of another reduced sensitizer or towards catalyst activation (see SI).[85,87]

$$[Ru(bpy)_3]^{2+} + h\nu \rightarrow *[Ru(bpy)_3]^{2+} \quad (8)$$

$$*[Ru(bpy)_3]^{2+} + DIPEA \rightarrow [Ru(bpy)_3]^{+} + DIPEA^{\bullet+} \quad (9)$$

$$[Ru(bpy)_3]^{+} + C_{ox} \rightarrow [Ru(bpy)_3]^{2+} + C_{red} \quad (10)$$

Table 2. Summary of photocatalytic data in acetonitrile.[a]

			n / μmol (TON) [b]			Selectivity [c] / %			TOF / h^{-1} (Φ / %) [d]		
Entry	Cat	H_2O / %	H_2	CO	Formate	H_2	CO	Formate	H_2	CO	Formate
1	**1** (50 μM)	1	34.0 (136)	4.5 (18)	1.5 (6)	85	11	4	37.7 (0.35)	7.9 (0.07)	n.d.
2	**1** (50 μM)	10	38.1 (152)	3.5 (14)	1.4 (6)	89	8	3	60.1 (0.50)	4.8 (0.04)	n.d.
3	**1** (10 μM)	10	38.6 (772)	3.6 (71)	1.8 (35)	88	8	4	2022 (0.70)	30 (0.05)	n.d.
4	**2** (50 μM)	1	2.4 (9)	43.3 (173)	4.6 (18)	5	86	9	4.7 (0.04)	65.5 (0.55)	n.d.
5	**2** (50 μM)	10	2.7 (11)	44.0 (176)	3.5 (14)	5	88	7	6.7 (0.05)	97.7 (0.85)	n.d.
6	**2** (10 μM)	10	9.0 (180)	18.6 (372)	1.4 (28)	31	64	5	141 (0.25)	240 (0.40)	n.d.
7	-	10	0.1 (-)	0.9 (-)	3.1 (-)	2	22	76	-	-	-

[a] Visible light irradiation (400-800 nm, 1 sun), 0.4 mM $[Ru(bpy)_3](PF_6)_2$, 0.1 M DIPEA, the data reported are averages of two independent experiments; [b] estimated after 5 h irradiation; [c] estimated as the ratio between the amount of a single product and the total amount of products; [d] estimated in the linear portion of the kinetic trace (see SI); n.d. = not determined.

Figure 8 depicts the kinetics of H_2 and CO formation upon 1 sun irradiation of acetonitrile solutions containing 0.4 mM $[Ru(bpy)_3](PF_6)_2$, 0.1 M DIPEA, and 50 μM complexes **1** and **2** as the catalysts in the presence of 10% H_2O. For both compounds we also tested a lower concentration and a lower water content and the resulting kinetics are reported in Section S5 of the SI (Figure S29-S32). Photochemical experiments conducted in the presence of 1 mL Hg yielded comparable kinetic profiles, supporting the molecular nature of the catalytic species.

A close inspection of the photocatalytic data collected in Table 2 immediately points towards a different catalytic behavior of the two complexes **1** and **2**. Under all the conditions tested the cobalt complex **1** brings to the formation of H_2 as the major product, while CO is obtained only as a minor product. A decrease of the water content from 10% to 1% (entries 1,2) only leads to a slight decrease of the selectivity for H_2 (from 89% to 85%) with the concurrent increase in the amount of CO. Changing the catalyst concentration from 50 to 10 μM (entries 2,3) has no remarkable impact on the activity and selectivity of the photochemical system, although a gain in both maximum TON and TOF values can be attained at lower catalyst concentrations (TON = 772, TOF = 2022 h^{-1} and TON = 71, TOF = 30 h^{-1} are recorded for the generation of H_2 and CO, respectively). In this respect, the similar quantum yield of hydrogen formation recorded at 10 and 50 μM can be possibly ascribed to the inefficient electron transfer quenching of the excited $[Ru(bpy)_3]^{2+}$ sensitizer by the DIPEA electron donor (eqs. 8,9), as previously established using Stern-Volmer analysis, which likely makes photogeneration of the $[Ru(bpy)_3]^{+}$ reductant the rate-limiting step of the photochemical process. In all experiments with **1**, formate is also detected as a photochemical product with a selectivity of 3-4%. Its amount is, however, in the order of the quantity measured in a blank experiment without any catalyst present (entry 7) and possibly suggests that its formation arises from the decomposition of the $[Ru(bpy)_3]^{2+}$ sensitizer to catalytically active species during photolysis, as already reported.[87,88]

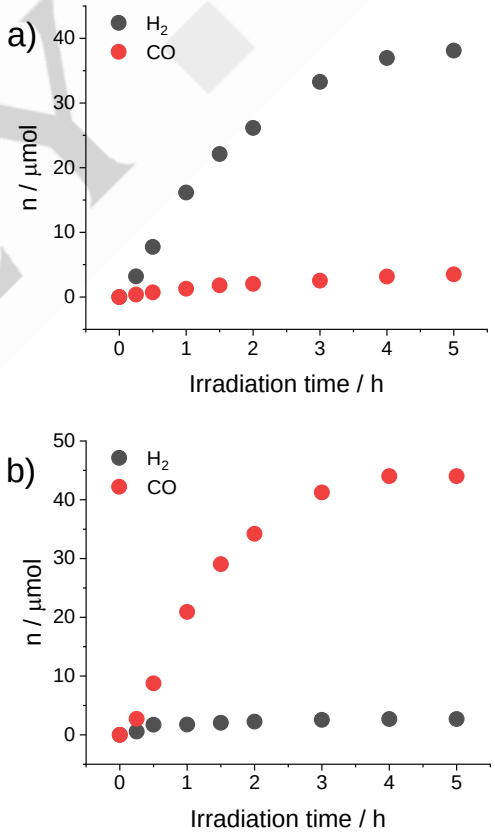

Figure 8. Kinetics of H_2 and CO formation upon continuous visible irradiation (400-800 nm, 1 sun) of acetonitrile solutions containing 0.4 mM $[Ru(bpy)_3](PF_6)_2$, 0.1 M DIPEA, 10% H_2O, and 50 μM a) complex **1** and b) complex **2**.

The failure to observe substantial formation of formate in the photochemical experiments and the net increase in the selectivity towards H_2 is noteworthy. This can be ascribed to the presence of acids other than water/carbonic acid in the photochemical

mixture due to the degradation of the one-electron oxidized species of the DIPEA donor, as previously inferred.[85,87] Formation of a hydride species (dictating the selectivity towards either CO or H_2, viz. pathway A vs B in Scheme 2) and the reaction of a hydride with CO_2 (impacting on the selectivity towards either H_2 or formate) are indeed strongly dependent on the pK_a of the acid source.[85,89] Moreover, stronger acids may also unlock a parallel ECEC mechanism towards hydrogen formation involving protonation of the Co(I) species, as previously reported.[64,65]

Differently from its parent cobalt complex, the iron complex **2** behaves as an efficient and selective catalyst for the reduction of CO_2 to CO. At a catalyst concentration of [**2**] = 50 μM and 10% H_2O (entry 5), CO is indeed formed as the major product with a selectivity of 88% and a quantum yield of Φ = 0.85%. Akin to the cobalt case, no strong differences were observed at lower water content (entries 4, 5). At 1% H_2O only a slight decrease of both the TOF and quantum yield of CO formation is indeed recorded, likely associated with the lower catalytic rate of complex **2** under this condition. Interestingly, a slight decrease in the selectivity of CO formation (from 88% to 64%) is attained at 10% H_2O when the catalyst concentration is lowered down to 10 μM (entries 4, 6). Similar to the cobalt case, formate is also evidenced as a photochemical product under all the conditions tested with a selectivity ranging between 5-9% (entries 4-6). Although the overall amount is generally larger than that measured under photolysis conditions using complex **1** (entries 1-3), the comparable quantity revealed in the blank experiment (entry 7), strongly suggests that formate production through catalysis by the iron complex represents a minor pathway.[87,88]

Even in the case of **2**, the similar overall quantum yields for product formation (i.e., sum of the Φ for both H_2 and CO) suggests that photocatalysis is limited by the choice of the sensitizer/donor couple. We would like to emphasize, however, that, besides these limitations, the photocatalytic performance of **2** is remarkable when compared to other iron complexes reported in the literature,[28] particularly taking into account, as a relevant figure-of-merit of the photochemical system, the maximum amount (i.e., moles) of CO product.[90,91] Although much room for improvement can be still envisioned for photochemical CO_2RR using this complex (e.g., by taking advantage of novel sensitizers and solvent environments[92] or via combination with other proton sources and/or sacrificial electron donors)[86] the photochemical data here reported represent one of the first examples in which a simple change of the metal center from cobalt to iron allows to drastically switch the reduction product while preserving a considerable catalytic response in terms of solar fuel formation, pointing out the critical role of the ligand in assisting catalysis promoted at the metal center. As a matter of fact, highly efficient and selective CO production was reported for the iron complex with a terpyridine-based ligand, but replacing the iron with cobalt resulted in poor HER activity under photochemical conditions associated with rapid catalyst decomposition.[50] Similarly, while selective CO_2RR to CO was recorded for an iron complex featuring a N,N,N-pincer ligand, inefficient H_2 formation was instead observed with the cobalt analog.[27]

Conclusion

We have investigated the catalytic activity of the cobalt (**1**) and iron (**2**) complexes of the hexadentate DBPy-PyA ligand towards the CO_2RR in acetonitrile/water mixtures. Under bulk electrolysis conditions the cobalt complex **1** displays poor selectivity towards the formation of CO while leading to the preferential formation of formate or hydrogen. On the other hand, the iron complex **2** is highly selective towards the generation of CO. This trend is further confirmed under photochemical conditions where H_2 and CO are detected as the major products in the case of **1** and **2**, respectively, thus pointing out completely different catalytic behaviors resulting from the simple change of the metal center. The different catalytic activity mainly stems from the strong propensity of the iron complex **2** to react with CO_2 rather than with H^+. Conversely, in the case of the cobalt analog **1** a similar thermodynamic driving force is observed in both the reaction with CO_2 and H+, suggesting a kinetic origin in the preferential reactivity shown by this latter. Further theoretical studies including the assessment of the energetics of all reaction intermediates and the calculation of the activation barriers for CO_2 and proton addition, have been already planned to better rationalize the different reactivity of **1** and **2** towards the CO_2RR and will be reported in due course. Nevertheless, the data presented in this work are strong proofs of the privileged role of the hexadentate DBPy-PyA ligand for the construction of active molecular catalysts for solar fuel formation, taking advantage of its flexibility and non-innocent redox behavior. Furthermore, the synthetic ease and tunability of this type of polypyridine ligands and their rational combination with different metal centers will definitely allow the preparation of a wide library of molecular catalysts to target specific, relevant transformations in the realm of Artificial Photosynthesis. Research towards these directions is currently planned in our labs.

Experimental Section

Materials and methods. All reagents were purchased from standard suppliers and used without further purification. $[Ru(bpy)_3](PF_6)_2$ was obtained by metathesis from the chloride salt. The latter was prepared according to literature procedures and recrystallized from water before precipitation with hexafluorophosphoric acid.[93] Ligand DBPy-PyA and complex **1** were obtained according to the previously reported procedure.[63] ^{1}H-NMR spectra were recorded on a Bruker Avance III 400 MHz instrument. High resolution mass spectra (HR-ESI) were obtained with a Dionex Ultimate 3000 UHPLC system (ThermoFischer Scientifics, Germering, Germany) connected to a QExactive MS with a heated ESI source (ThermoFisher Scientific, Bremen, Germany). CHN Elemental Analysis was performed with a Unicube (Elementar) micro elemental analyser. X-ray diffraction data were acquired on a single crystal of complex **2** mounted on loop with oil using a STOE IPDS II diffractometer. The crystal was kept at 250(2) K during data collection. Using Olex2,[94] the structure was solved with the SHELXT[95] structure solution program using Intrinsic Phasing and refined with the SHELXL[96] refinement package using Least Squares minimization. The number of unpaired electrons in complex **2** in acetonitrile-d_3 was calculated by using the Evans method according to a literature procedure.[97] Electronic absorption spectra were recorded at room temperature on an Agilent Technologies spectrophotometer. Time-resolved luminescence was performed with a custom laser spectrometer comprised of a Continuum Surelite II Nd:YAG laser (FWHM = 8 ns) with frequency doubled (532 nm, 330 mJ) option.

Signals from the photomultiplier (kinetic traces) were processed by means of a TeledyneLeCroy 604Zi (400 MHz, 20 GS/s) digital oscilloscope.

Electrochemistry. Cyclic voltammetry (CV) measurements were carried out on a PGSTAT 302N potentiostat (Autolab) in a three-electrode cell, using a glassy carbon as the working electrode, a silver wire as the quasi-reference electrode and a Pt wire as counter electrode. $TBAPF_6$ was employed as the supporting electrolyte. Solutions were purged for 20 min with either N_2 or CO_2 prior to analysis. Potential controlled electrolysis experiments were performed in a gas-tight custom-made electrochemical cell using a high-surface area glassy carbon rod as the working electrode, a platinum wire as the counter electrode (separated from the test solution by a frit) and SCE as the reference electrode (potentials were converted vs. Fc^+/Fc for uniformity with CV experiments by subtracting 0.4 V).[98] The head-space of the cell was connected to a gas-chromatography (GC) apparatus (see below for details) for the determination and quantification of H_2 and CO. The bulk electrolysis experiments were run in duplicate and the results reported are averages of two independent experiments. Spectroelectrochemistry was performed using a commercial OTTLE cell (ProSense) using a Pt grid as the working electrode, a silver wire as the quasi-reference electrode and a Pt wire as counter electrode. Potentials were referenced to Fc^+/Fc by addition of ferrocene at the end of the experiment.

Photochemistry. The photocatalysis experiments were carried out upon continuous visible light irradiation with a 175 W xenon arc-lamp (CERMAX PE175BFA) of a reactor containing the solution (a 10 mm pathlength pyrex glass cuvette with head space obtained from a round-bottom flask). A cut-off filter at 400 nm and a hot mirror (IR filtering) have been used to provide the useful wavelength range (400-800 nm). An incident power of 1 sun (100 mW/cm^2) was set using a power meter. In a typical photochemical experiment, samples of 5 mL were prepared in 20 mL scintillation vials by mixing mother solutions of $[Ru(bpy)_3](PF_6)_2$ and the catalyst, followed by addition of water and DIPEA. The solution was then put in the reactor, bubbled with CO_2 for 20 min and kept at a constant temperature of ca 15°C. The cell was then irradiated and the solution continually stirred during the photolysis. The photochemical experiments were run in duplicate and the results reported are averages of two independent experiments.

Detection of reduction products. The gas products, namely H_2 and CO, were detected and quantified using a GC apparatus. The measuring cell (either the bulk electrolysis or photochemical cell) is sealed during the photoreaction: the head to which the cell is attached has four ports, closed with Swagelok® connections, two of them are part of a closed loop involving GC gas inlet and sample vent to analyse the head space content without an appreciable gas consumption, and the other two are for the degassing procedure (input and output). The gas phase of the reaction vessel was analyzed on an Agilent Technologies 490 microGC equipped with a 5 Å molecular sieve column (10 m), a thermal conductivity detector, and using Ar as carrier gas. The unused gas sample is then reintroduced in the reactor to minimize its consumption along the whole photolysis. The amount of gases was quantified through the external calibration method. In the case of H_2, this procedure was performed through a galvanostatic (typically 1 mA) electrolysis of a 0.1 M H_2SO_4 solution. A 100% faradaic efficiency was assumed leading to a linear correlation between the amount of H_2 evolved at the cathode and the electrolysis time. CO was quantified using a response factor obtained by injecting known amounts of gas in the cell and then sampling the headspace. Average errors were within ±10% for CO and ±5% for H_2. An example of GC analysis output is reported in the Supporting Information (Figure S34). Formate was quantified using ^{1}H-NMR (δ = 8.3 ppm). The electrolyzed or photolyzed solutions were brought to basic pH upon addition of the minimum amount of NaOH and then evaporated under reduced pressure. The solid residue was then dissolved in 2 mL D_2O and sonicated for 5 min, dimethylformamide (typically 1-2 μL, δ = 7.8 ppm) was then added as an internal standard and the resulting solution filtered before entering the NMR tube. An example of NMR analysis for formate detection is reported in the SI (Figure S35).

Theoretical calculations. After a preliminary benchmark investigation, detailed in Section S3 in the SI, the B3LYP/6-311G* approach was selected to calculate the equilibrium structures and the electronic structure of complex **2** and its reduction products. Solvent effects were accounted for by using the CPCM approach, as implemented in Gaussian16.[99] Redox potentials in acetonitrile for complex **2** were calculated as free energy differences in solution obtained by following the proper thermodynamic cycle, as detailed in our previous works.[64,65,67,100] The absolute potentials calculated vs. vacuum were converted vs. Fc^+/Fc by adding −4.80 V.[101] The exchange coupling constants for the HS (ferromagnetic) LS (antiferromagnetic) states were calculated following literature protocols[102] according to eq 11 at B3LYP/6-311G* level of theory, using the calculated adiabatic free energy differences in acetonitrile.

$$J_{ab} = (E_{HS} - E_{LS}) / {}^{HS}\langle S^2\rangle - {}^{LS}\langle S^2\rangle \qquad (11)$$

The driving forces for the formation of the proposed Co(II)-COOH and Co(II)-H (Scheme 2) and Fe(II)-COOH and Fe(II)-H (Scheme 3) intermediated, were calculated as free energy changes in solution for the reactions M(0) $+H^+ \rightarrow$ M(II)-H and M(0) $+ H^+ + CO_2 \rightarrow$ M(II)-COOH, using a value of $G^*(H^+_{(s)})$ = −266.5 kcal/mol, coherently with the approach adopted in our previous works.[64,65,67] UV-Vis absorption spectra were obtained by Gaussian convolution of the vertical excitation energies (FWHM of 0.17 eV) calculated by Time-Dependent DFT (TD-DFT) for complex **2** and its formal Fe(I) and Fe(0) species in their lowest energy spin states, namely S=2, S=3/2 (antiferromagnetic solution) and S=1 (antiferromagnetic solution), respectively.

Synthesis and characterization of complex 2. Complex **2** was obtained by reaction of 250 mg of DBPy-PyA ligand (0.56 mmol) dissolved in 30 mL of methanol with 206 mg of $Fe(BF_4)_2.6H_2O$ (0.61 mmol) dissolved in 2 mL of methanol under air-equilibrated conditions. The resulting solution was stirred overnight, filtered and precipitated with diethylether to give 290 mg (0.41 mmol; 73% yield) of pure complex **2**. HR-ESI (m/z): 250.0705 $[M-2BF_4]^{2+}$ (calc. for $C_{28}H_{24}N_6Fe^{2+}$: 250.0700). Elemental analysis: calc. % for $C_{26}H_{28}B_2F_8FeN_6O$ (M+MeOH): C 49.33, H 4.00, N 11.90; found C 49.06, H 3.78, N 12.19. Crystal Data for **2** (M = 738.08 g/mol): monoclinic, space group $C_{2/c}$ (no. 15), a = 26.5556(14) Å, b = 12.5792(5) Å, c = 24.8518(13) Å, β = 127.612(3)°, V = 6576.3(6) Å^3, Z = 8, T = 250(2) K, μ(Mo Kα) = 0.543 mm^{-1}, Dcalc = 1.491 g/cm^3, 30338 reflections measured (3.544° ≤ 2Θ ≤ 52.49°), 6557 unique (Rint = 0.0834, Rsigma = 0.0538) which were used in all calculations. The final R1 was 0.0837 (I > 2σ(I)) and wR2 was 0.2650 (all data). CCDC 224776 contains the supplementary crystallographic data for this article. These data can be obtained free of charge from The Cambridge Crystallographic Data Centre via https://www.ccdc.cam.ac.uk/structures/

Acknowledgements

M.N. acknowledges financial support from the University of Ferrara (FAR2021, FAR2022). A.A. acknowledges the grant from the Italian MUR (PRIN project 2020927WY3_001 - ElectroLight4Value). A.R. acknowledges the University of Fribourg for financial support. M.P. acknowledges HPC resources from mesocentre EXPLOR of the University of Lorraine (project 2018CPMXX0602). Marco Carmosino (University of Ferrara) is gratefully acknowledged for lab assistance.

Keywords: CO_2 reduction • homogeneous catalysis • iron(II) complex • cobalt(II) complex • artificial photosynthesis

[1] A. Morris, G. J. Meyer, E. Fujita, *Acc. Chem. Rev*. **2009**, *42*, 1983-1994.

[2] J. L. White, M. F. Baruch, J. E. Pander III, Y. Hu, I. C. Fortmeyer, J. E. Park, T. Zhang, K. Liao, J. Gu, Y. Yan, T. W. Shaw, E. Abelev, A. B. Bocarsly, *Chem. Rev.* **2015**, *115*, 12888-12935.

[3] H. Takeda, C. Cometto, O. Ishitani, M. Robert, *ACS Catal.* **2017**, *7*, 70-88.

[4] E. E. Benson, C. P. Kubiak, A. Sathrum, J. M. Smieja, *Chem. Soc. Rev.* **2009**, *38*, 89-99.

[5] E. Lamy, L. Nadjo, J.-M. Savéant, *J. Electroanal. Chem.* **1977**, *78*, 403-407.

[6] N. Sutin, C. Creutz, E. Fujita, *Comments Inorg. Chem.* **1997**, *19*, 67-92.

[7] H. Takeda, K. Koike, H. Inoue, O. Ishitani, *J. Am. Chem. Soc.* **2008**, *130*, 2023-2031.

[8] T. Nakajima, Y. Tamaki, K. Ueno, E. Kato, T. Nishikawa, K. Ohkubo, Y. Yamazaki, T. Morimoto, O. Ishitani, *J. Am. Chem. Soc.* **2016**, *138*, 13818-13821.

[9] J. M. Smeja, C. P. Kubiak, *Inorg. Chem.* **2010**, *49*, 9283-9289.

[10] J. A. Keith, K. A. Grice, C. P. Kubiak, E. A. Carter, *J. Am. Chem. Soc.* **2013**, *135*, 15823-15829.

[11] L. Rotundo, C. Garino, E. Priola, D. Sassone, H. Rao, B. Ma, M. Robert, J. Fiedler, R. Gobetto, C. Nervi, *Organometallics* **2019**, *38*, 1351-1360.

[12] Y. Tamaki, K. Koike, O. Ishitani, *Chem. Sci.* **2015**, *6*, 7213-7221.

[13] R. Kuriki, H. Matsunaga, T. Nakashima, K. Wada, A. Yamakata, O. Ishitani, K. Maeda, *J. Am. Chem. Soc.* **2016**, *138*, 5159-5170.

[14] P. Kang, Z. Chen, A. Nayak, S. Zhang, T. J. Meyer, *Energy Environ. Sci.* **2014**, *7*, 4007-4012.

[15] S. Gonell, E. A. Assaf, K. D. Duffee, C. K. Schauer, A. J. M. Miller, *J. Am. Chem. Soc.* **2020**, *142*, 8980-8999.

[16] B. A. Johnson, S. Maji, H. Agarwala, T. A. White, E. Mijangos, S. Ott, *Angew. Chem. Int. Ed.* **2016**, *55*, 1825-1829.

[17] M. D. Sampson, A. D. Nguyen, K. A. Grice, C. E. Moore, A. L. Rheingold, C. P. Kubiak, *J. Am. Chem. Soc.* **2014**, *136*, 5460-5471.

[18] M. D. Sampson, C. P. Kubiak, *J. Am. Chem. Soc.* **2016**, *138*, 1386-1393.

[19] F. Franco, M. F. Pinto, B. Royo, J. Lloret-Fillol, *Angew. Chem. Int. Ed.* **2018**, *57*, 4603-4606.

[20] B. Reuillard, K. H. Ly, T. E. Rosser, M. F. Kuehnel, I. Zebger, E. Reisner, *J. Am. Chem. Soc.* **2017**, *139*, 14425-14436.

[21] X. Zhang, M. Cibian, A. Call, K. Yamauchi, K. Sakai, *ACS Catal.* **2019**, *9*, 11263-11273.

[22] Z. Guo, G. Chen, C. Cometto, B. Ma, H. Zhao, T. Groizard, L. Chen, H. Fan, W. L. Man, S. M. You, K. C. Lau, T. C. Lau, M. Robert, *Nat. Catal.* **2019**, *2*, 801-808.

[23] L. Chen, Z. Guo, X. G. Wei, C. Gallenkamp, J. Bonin, E. Anxolabéhère-Mallart, K. C. Lau, T. C. Lau, M. Robert, *J. Am. Chem. Soc.* **2015**, *137*, 10918-10921.

[24] S. Gonell, J. Lloret-Fillol, A. J. M. Miller, *ACS Catal.* **2021**, *11*, 615-626.

[25] R. Bonetto, R. Altieri, M. Tagliapietra, A. Barbon, M. Bonchio, M. Robert, A. Sartorel, *ChemSusChem* **2020**, *13*, 4111-4120.

[26] R. Bonetto, D. Civettini, F. Crisanti, A. Sartorel, *Energies* **2021**, *14*, 5723.

[27] L. L. Gracia, E. Barani, J. Braun, A. B. Carter, O. Fuhr, A. K. Powell, K. Fink, C. Bizzarri, *ChemCatChem* **2022**, *14*, e202201163.

[28] C. Bizzarri, *Eur. J. Org. Chem*. **2022**, e202200185.

[29] K. Kosugi, H. Kashima, M. Kondo, S. Masaoka, *Chem. Commun.* **2022**, *58*, 2975-2978.

[30] S. L. Hooe, J. M. Dressel, D. A. Dickie, C. W. Machan, *ACS Catal.* **2020**, *10*, 1146-1151.

[31] I. Azcarate, C. Constentin, M. Robert, J.-M. Savéant, *J. Am. Chem. Soc.* **2016**, *138*, 16639-16644.

[32] I. Azcarate, C. Constentin, M. Robert, J.-M. Savéant, *J. Phys. Chem. C* **2016**, *120*, 28951-28960.

[33] C. G. Margarit, N. G. Asimov, C. Constentin, D. G. Nocera, *ACS Energy Lett.* **2020**, *5*, 72-78.

[34] S. Amanullah, P. Saha, A. Dey, *J. Am. Chem. Soc.* **2021**, *143*, 13579-13592.

[35] K. Guo, X. Li, H. Tao, H. Guo, X. Jin, X. P. Zhang, W. Zhang, U. P. Apfel, R. Cao, *Angew. Chem. Int. Ed.* **2022**, *61*, e202209602.

[36] R. Cao, *ChemSusChem* **2022**, *15*, e202201788.

[37] E. M. Nichols, J. S. Derrick, S. K. Nistanaki, P. T. Smith, C. J. Chang, *Chem. Sci*. **2018**, *9*, 2952-2960.

[38] A. W. Nichols, S. L. Hooe, J. S. Kuehner, D. A. Dickie, C. W. Machan, *Inorg. Chem.* **2020**, *59*, 5854-5864.

[39] D. Z. Zee, M. Nippe, A. E. King, C. J. Chang, J. R. Long, *Inorg. Chem*. **2020**, *59*, 5206-5217.

[40] W. Nie, D. E. Tarnopol, C. C. L. McCrory, *J. Am. Chem. Soc.* **2021**, *143*, 3764-3778.

[41] D. C. Liu, H. J. Wang, T. Ouyang, J. W. Wang, L. Jiang, D. C. Zhong, T. B. Lu, *ACS Appl. Energy Mater.* **2018**, *1*, 2452-2459.

[42] W. Xia, Y. Y. Ren, J. Liu, B. Y. Deng, F. Wang, *J. Photochem. Photobio A: Chem*. **2022**, *426*, 113754.

[43] D. Hong, T. Kawanishi, Y. Tsukakoshi, H. Kotani, T. Ishizuka, T. Kojima, *J. Am. Chem. Soc*. **2019**, *141*, 20309-20317.

[44] L. E. Lieske, A. L. Rheingold, C. W. Machan, *Sustainable Energy Fuels* **2018**, *2*, 1269-1277.

[45] N. Elgrishi, M. B. Chambers, V. Artero, M. Fontecave, *Phys. Chem. Chem. Phys.* **2014**, *16*, 13635-13644.

[46] N. Elgrishi, M. B. Chambers, M. Fontecave, *Chem. Sci*. **2015**, *6*, 2522-2531.

[47] M. Bourrez, F. Molton, S. Cardon-Noblat, A. Deronzier, *Angew. Chem. Int. Ed.* **2011**, *50*, 9903-9906.

[48] M. Bourrez, M. Orio, F. Molton, H. Vezin, C. Duboc, A. Deronzier, S. Chardon-Noblat, *Angew. Chem. Int. Ed.* **2014**, *53*, 240-243.

[49] J.-S. Derrick, M. Loipersberger, R. Chatterjee, D. A. Iovan, P. T. Smith, K. Chakarawet, J. Yano, J. R. Long, M. Head-Gordon, C. J. Chang, *J. Am. Chem. Soc.* **2020**, *142*, 20489-20501.

[50] P. De La Torre, J. S. Derrick, A. Snider, P. T. Smith, M. Loipersberger, M. Head-Gordon, C. J. Chang, *ACS Catal.* **2022**, *12*, 8484-8493.

[51] N. Queyriaux, *ACS Catal*. **2021**, *11*, 4024-4035.

[52] N. Queyriaux, K. Abel, J. Fize, J. Pécaut, M. Orio, L. Hammarström, *Sustainable Energy Fuels* **2020**, *4*, 3668-3676.

[53] W. Nie, C. C. L. McCrory, *Chem. Commun*. **2018**, *54*, 1579-1582.

[54] L. Duan, G. F. Manbeck, M. Kowalczyk, D. J. Szalda, J. T. Muckerman, Y. Himeda, E. Fujita, *Inorg. Chem.* **2016**, *55*, 4582-4594.

[55] M. Natali, R. Argazzi, C. Chiorboli, E. Iengo, F. Scandola, *Chem. Eur. J.* **2013**, *19*, 9261-9271.

[56] M. Natali, M. Orlandi, C. Chiorboli, E. Iengo, V. Bertolasi, F. Scandola, *Photochem. Photobio. Sci.* **2013**, *12*, 1749-1753.

[57] M. Natali, A. Luisa, E. Iengo, F. Scandola, *Chem. Commun.* **2014**, *50*, 1842-1844.

[58] E. Deponti, A. Luisa, M. Natali, E. Iengo, F. Scandola, *Dalton Trans*. **2014**, *43*, 16345-16353.

[59] M. Natali, E. Badetti, E. Deponti, M. Gamberoni, F. A. Scaramuzzo, A. Sartorel, C. Zonta, *Dalton Trans*. **2016**, *45*, 14764-14773.

[60] N. A. Carmo dos Santos, M. Natali, E. Badetti, K. Wurst, G. Licini, C. Zonta, *Dalton Trans*. **2017**, *46*, 16455-16464.

[61] E. Benazzi, F. Begato, A. Niorettini, L. Destro, K. Wurst, G. Licini, S. Agnoli, C. Zonta, M. Natali, *J. Mater. Chem. A* **2021**, *9*, 20032-20039.

[62] F. Droghetti, F. Lucarini, A. Molinari, A. Ruggi, M. Natali, *Dalton Trans.* **2022**, *51*, 10658-10673.

[63] F. Lucarini, M. Pastore, S. Vasylevskyi, M. Varisco, E. Solari, A. Crochet, K. M. Fromm, F. Zobi, A. Ruggi, *Chem. Eur. J.* **2017**, *23*, 6768-6771.

[64] F. Lucarini, J. Fize, A. Morozan, M. Marazzi, M. Natali, M. Pastore, V. Artero, A. Ruggi, *Sustainable Energy Fuels* **2020**, *4*, 589-599.

[65] F. Lucarini, D. Bongni, P. Schiel, G. Bevini, E. Benazzi, E. Solari, F. Fadaei-Tirani, R. Scopelliti, M. Marazzi, M. Natali, M. Pastore, A. Ruggi, *ChemSusChem* **2021**, *14*, 1874-1885.

[66] A. Orlando, F. Lucarini, E. Benazzi, F. Droghetti, A. Ruggi, M. Natali, *Molecules* **2022**, *27*, 8277.

[67] F. Lucarini, J. Fize, A. Morozan, F. Droghetti, E. Solari, R. Scopelliti, M. Marazzi, M. Natali, M. Pastore, V. Artero, A. Ruggi, *Sustainable Energy Fuels* **2023**, *7*, 3384-3394.

[68] D. L. DuBois, *Inorg. Chem*. **2014**, *53*, 3935-3960.

[69] M. W. Drover, *Chem. Soc. Rev.* **2022**, *51*, 1861-1880.

[70] Results of a research in the CCDC performed on 28.04.2023 excluding porphyrinoid ligands and CN^- as seventh ligand.

[71] N. E. Brese, M. O'Keeffe, *Acta Crystallogr. Sect. A* **1991**, *47*,192-197.

[72] I. D. Brown, *The Chemical Bonding Inorganic Chemistry: The Bond Valence Model*, **2002**, Oxford University Press, Oxford.

[73] Y. Nelyubina, A. Polezhaev, A. Pavlov, D. Aleshin, S. Savkina, N. Efimov, T. Aliev, V. Novikov, *Magnetochemistry* **2018**, *4*, 46.

[74] M. Pastore, E. Mosconi, F. De Angelis, M. Grätzel, *J. Phys. Chem. C* **2010**, *114*, 7205-7212.

[75] M. Pastore, S. Fantacci, F. De Angelis, *J. Phys. Chem. C* **2013**, *117*, 3685-3700.

[76] M. Pastore, F. De Angelis, *J. Am. Chem. Soc.* **2015**, *137*, 5798-5809.

[77] A. M. Brown, C. E. McCusker, J. K. McCusker, *Dalton Trans*. **2014**, *43*, 17635-17646.

[78] Y. Tomita, S. Teruya, O. Koga, Y. Hori, *J. Electrochem. Soc.* **2000**, *147*, 4164-4167.

[79] V. Fourmond, P. A. Jacques, M. Fontecave, V. Artero, *Inorg. Chem.* **2010**, *49*, 10338-10347.

[80] J.-M. Savéant, *Elements of Molecular and Biomolecular Electrochemistry: An Electrochemical Approach to Electron Transfer Chemistry*, **2006**, John Wiley & Sons, Inc.

[81] N. Queyriaux, D. Sun, J. Fize, J. Pécaut, M. J. Field, M. Chavarot-Kerlidou, V. Artero, *J. Am. Chem. Soc.* **2020**, *142*, 274-282.

[82] S. Fernandez, F. Franco, C. Casadevall, V. Martin-Diaconescu, J. M. Luis, J. Lloret-Fillol, *J. Am. Chem. Soc.* **2020**, *142*, 120-133.

[83] C. Costentin, S. Drouet, M. Robert, J.-M. Savéant, *J. Am. Chem. Soc.* **2012**, *134*, 11235-11242.

[84] C. Constentin, J.-M. Savéant, *ChemElectroChem* **2014**, *1*, 1226-1236.

[85] R. Bonetto, F. Crisanti, A. Sartorel, *ACS Omega* **2020**, *5*, 21309-21319.

[86] Y. Pellegrin, F. Odobel, *C. R. Chimie* **2017**, *20*, 283-295.

[87] T. Shimoda, T. Morishima, K. Kodama, T. Hirose, D. E. Polyansky, G. F. Manbeck, J. T. Muckerman, E. Fujita, *Inorg. Chem.* **2018**, *57*, 5486-5498.

[88] J. M. Lehn, R. Ziessel, *J. Organometall. Chem.* **1990**, *382*, 157-173.

[89] K. M. Waldie, A. L. Ostericher, M. H. Reineke, A. F. Sasayama, C. P. Kubiak, *ACS Catal*. **2018**, *8*, 1313-1324.

[90] We would like to point out that the modest quantum yields here estimated are the result of the use of a polychromatic irradiation source (see SI). Larger quantum yields have been reported in other photocatalytic systems using monochromatic light in spite of the generation of lower amounts of CO product and at lower production rates. It is indeed documented that the quantum yield in complex photochemical reactions may strongly depend on the irradiation power.[91]

[91] A. Volpe, C. Tubaro, M. Natali, A. Sartorel, G. W. Brudvig, M. Bonchio, *Inorg. Chem*. **2019**, *58*, 16537-16545.

[92] E. Bassan, R. Inoue, D. Fabry, F. Calogero, S. Potenti, A. Gualandi, P. G. Cozzi, K. Kamogawa, P. Ceroni, Y. Temaki, O. Ishitani, *Sustainable Energy Fuels* **2023**, *7*, 3454-3463.

[93] J. A. Broomhead, C. G. Young, P. Hood, *Inorg. Synth*. **1990**, *28*, 338-340.

[94] O. V. Dolomanov, L. J. Bourhis, R. J. Gildea, J. A. K. Howard, H. Puschmann, *J. Appl. Cryst*. **2009**, *42*, 339-341.

[95] G. M. Sheldrick, *Acta Cryst*. **2015**, *A71*, 3-8.

[96] G. M. Sheldrick, *Acta Cryst*. **2015**, *C71*, 3-8.

[97] Y. Nelyubina, A. Polezhaev, A. Pavlov, D. Aleshin, S. Savkina, N. Efimov, T. Aliev, V. Novikov, *Magnetochemistry* **2018**, *4*, 46.

[98] N. G. Connelly, W. E. Geiger, *Chem. Rev*. **1996**, *96*, 877-910.

[99] Gaussian 16, Revision C.01, M. J. Frisch, G. W. Trucks, H. B. Schlegel, G. E. Scuseria, M. A. Robb, J. R. Cheeseman, G. Scalmani, V. Barone, G. A. Petersson, H. Nakatsuji, X. Li, M. Caricato, A. V. Marenich, J. Bloino, B. G. Janesko, R. Gomperts, B. Mennucci, H. P. Hratchian, J. V. Ortiz, A. F. Izmaylov, J. L. Sonnenberg, D. Williams-Young, F. Ding, F. Lipparini, F. Egidi, J. Goings, B. Peng, A. Petrone, T. Henderson, D. Ranasinghe, V. G. Zakrzewski, J. Gao, N. Rega, G. Zheng, W. Liang, M. Hada, M. Ehara, K. Toyota, R. Fukuda, J. Hasegawa, M. Ishida, T. Nakajima, Y. Honda, O. Kitao, H. Nakai, T. Vreven, K. Throssell, J. A. Montgomery Jr., J. E. Peralta, F. Ogliaro, M. J. Bearpark, J. J. Heyd, E. N. Brothers, K. N. Kudin, V. N. Staroverov, T. A. Keith, R. Kobayashi, J. Normand, K. Raghavachari, A. P. Rendell, J. C. Burant, S. S. Iyengar, J. Tomasi, M. Cossi, J. M. Millam, M. Klene, C. Adamo, R. Cammi, J. W. Ochterski, R. L. Martin, K. Morokuma, O. Farkas, J. B. Foresman, D. J. Fox, **2016**, Gaussian, Inc., Wallingford CT.

[100] M. Pastore, S. Fantacci, F. De Angelis, *J. Phys. Chem. C* **2010**, *114*, 22742-22750.

[101] C. Fujisue, T. Kadoya, T. Higashino, R. Sato, T. Kawamoto, T. Mori, *RSC Adv.* **2016**, *6*, 53345-53350.

[102] T. Soda, Y. Kitagawa, T. Onishi, Y. Takano, Y. Shigeta, H. Nagao, Y. Yoshioka, K. Yamaguchi, *Chem. Phys. Lett.* **2000**, *319*, 223-230.

Entry for the Table of Contents

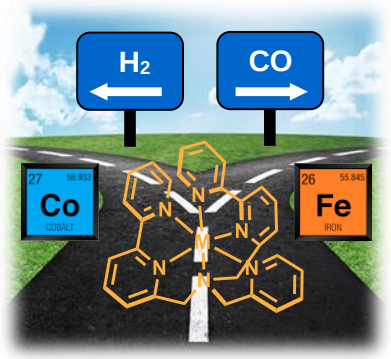

The metal makes the difference! Different reaction pathways are followed when CO_2 reduction is attempted in acetonitrile/water mixtures using either a cobalt(II) or an iron(II) molecular catalyst based on a hexadentate chelating ligand. This translates in preferred H_2/formate generation or CO formation employing the cobalt(II) or the iron(II) complex, respectively.